Anal. Chem. **2005,** *77,* 1911−1915

Lithographically Fabricated Nanopore-Based Electrodes for Electrochemistry

Serge G. Lemay,* Dennis M. van den Broek, Arnold J. Storm, Diego Krapf, Ralph M. M. Smeets, Hendrik A. Heering, and Cees Dekker

Kavli Institute of Nanoscience, Delft University of Technology, Lorentzweg 1, 2628 CJ Delft, The Netherlands

We report a new technique for fabricating electrodes for electrochemical applications with lateral dimensions in the range 15−200 nm and a reproducible, well-defined geometry. This technique allows determining the electrode size by electron microscopy prior to electrochemical measurements and without contamination of the metal electrode. We measured the diffusion-limited current with stepped-current voltammetry and showed that its dependence on electrode size can be quantitatively understood if the known geometry of the electrodes is explicitly taken into account.

The miniaturization of electrodes extends the capabilities of voltammetry as an analytical technique. This stems ultimately from the higher current densities and the shorter times needed to reach the diffusive steady state when using small electrodes.[1,2] Several techniques have been reported that allow fabricating electrodes with effective lateral dimensions as small as a few nanometers. A particularly successful approach consists of selectively coating atomically sharp metal tips with an insulator such as wax,[3−5] polyimide,[6] or electrophoretic paint.[7−14] Other examples of successful approaches include glass-sealed metal electrodes[15−19] focused-ion-beam sculpting,[20,21] silicon-based microfabrication techniques,[20−23] and carbon nanofibers[24] or carbon nanotubes[25] coated with an insulator. Several techniques have been employed to deduce partial geometry information on these electrodes, for example, analysis of scanning electrochemical microscopy approach curves[4,5] and independent measurements of both the surface area and the effective diffusion-limited radii of electrodes.[14] These studies revealed variations between electrodes fabricated using a nominally uniform process, indicating that quantitative analysis may require characterizing each electrode individually. This is impractical for routine work, in particular since the characterization techniques are not always compatible with further use of the electrodes.

Here we introduce a method for the controlled fabrication of nanoelectrodes using electron beam lithography and associated techniques, and demonstrate devices with lateral dimensions between 15 and 200 nm. The electrodes consist of a nanometer-scale opening in an insulated silicon membrane that is subsequently blocked on one side with metal. The main advantages of this technique are that the shape of the electrodes is reproducible for devices prepared using the same process, that this shape can be reliably characterized experimentally, and that the size of each individual electrode can be determined prior to—and independently from—electrochemical measurements. In addition, the metal of the electrode is never exposed to contaminants during fabrication and characterization. We present voltammetric data for electrodes of various sizes and show that the size dependence can be understood from the three-dimensional diffusion profile, provided that the known shape of the electrode is taken into account.

* Corresponding author: (e-mail) lemay@mb.tn.tudelft.nl; (tel) +31-15-2783220; (fax) +31-15-2781202.

(1) Zoski, C. G. *Electroanalysis* **2002**, *14*, 1041−1051.
(2) Bard, A. J.; Faulkner, L. R. *Electrochemical Methods, Fundamentals and Applications*, 2nd ed.; John Wiley & Sons: New York, 2001.
(3) Nagahara, L. A.; Thudat, T.; Lindsey, S. M. *Rev. Sci. Instrum.* **1989**, *60*, 3128−3130.
(4) Mirkin, M. V.; Fan, F. F.-R.; Bard, A. J. *J. Electroanal. Chem.* **1992**, *328*, 47−62.
(5) Fan, F. F.-R.; Kwak, J.; Bard, A. J. *J. Am. Chem. Soc.* **1996**, *118*, 9669−9675.
(6) Sun, P.; Zhang, Z.; Guo, J.; Shao, Y. *Anal. Chem.* **2001**, *73*, 5346−5351.
(7) Slevin, C. J.; Gray, N. J.; Macpherson, J. V.; Webb, M. A.; Unwin, P. R. *Electrochem. Commun.* **1999**, *1*, 282−288.
(8) Macpherson J. V.; Unwin P. R. *Anal. Chem.* **2000**, *72*, 276−285.
(9) Conyers, Jr. J. L.; White, H. S. *Anal. Chem.* **2000**, *72*, 4441−4446.
(10) Gray, N. J.; Unwin, P. R. *Analyst* **2000**, *125*, 889−893.
(11) Chen, S.; Kucernak, A. *Electrochem. Commun.* **2002**, *4*, 80−85.
(12) Chen, S.; Kucernak, A. *J. Phys. Chem. B* **2002**, *106*, 9396−9404.
(13) Abbou, J.; Demaille, C.; Druet, M.; Moiroux, J. *Anal. Chem.* **2002**, *74*, 6355−6363.
(14) Watkins, J. J.; Chen, J.; White, H. S., Abruna, H. D.; Maisonhaute, E.; Amatore, C. *Anal. Chem.* **2003**, *75*, 3962−3971.
(15) Penner, R. M.; Heben, M. J.; Longin, T. L.; Lewis, N. S. *Science* **1990**, *250*, 1118−1121.
(16) Pendley, B. D.; Abruna, H. D. *Anal. Chem.* **1990**, *62*, 782−784.
(17) Shao, Y. H.; Mirkin, M. V.; Fish, G.; Kokotov, S.; Palanker, D.; Lewis, A. *Anal. Chem.* **1997**, *69*, 1627−1634.
(18) Katemann, B. B.; Schuhmann, W. *Electroanalysis* **2002**, *14*, 22−28.
(19) Zhang, B.; Zhang, Y.; White, H. S. *Anal. Chem.* **2004**, *76*, 6229−6238.
(20) Kranz, C.; Friedbacher, G.; Mizaikoff, B.; Lugstein, A.; Smoliner, J.; Bertagnolli, E. *Anal. Chem.* **2001**, *73*, 2491−2500.
(21) Lugstein, A.; Bertagnolli, E.; Kranz, C.; Mizaikoff, B. *Surf. Interface Anal.* **2002**, *33*, 146−150.
(22) Thiébaud, P.; Beuret, C.; de Rooij, N. F.; Koudelka-Hep, M. *Sens. Actuators, B* **2000**, *70*, 51−56.
(23) Saenger, K. L.; Costrini, G.; Kotecki, D. E.; Kwietniak, K. T.; Andricacosa, P. C. *J. Electrochem. Soc.* **2001**, *148*, C758−C761.
(24) Guillorn, M. A.; McKnight, T. E.; Melechko, A.; Merkulov, V. I.; Britt, P. F.; Austin, D. W.; Lowndes, D. H.; Simpson, M. L. *J. Appl. Phys.* **2002**, *91*, 3824−3828.
(25) Campbell, J. K.; Sun, L.; Crooks, R. M. *J. Am. Chem. Soc.* **1999**, *121*, 3779−3780.

10.1021/ac0489972 CCC: $30.25 © 2005 American Chemical Society
Published on Web 02/15/2005

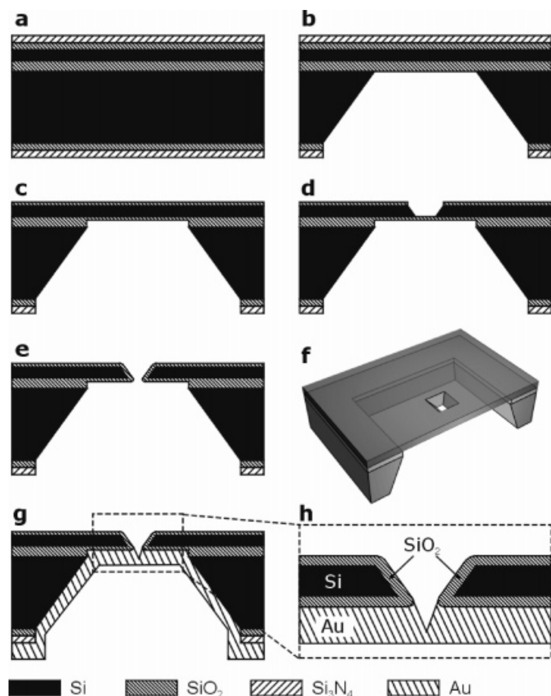

Figure 1. (a−e) Cross-sectional views of the electrodes at various stages of the fabrication process, as described in the text. (f) Three-dimensional, cross-sectional view of the structure at the stage depicted in (e). (g) After evaporating gold on one side, an electrode is formed in the aperture of the pore. (h) Detail of the final structure shown in (g).

EXPERIMENTAL SECTION

Electrode Fabrication. The electrodes were fabricated using standard processes from the semiconductor industry. In short, the pores were etched in silicon membranes using a process developed by Gribov et al.[26] The silicon surface of the pore and the membrane were then oxidized. Finally, electrodes were formed by deposition of a noble metal layer. The key steps in this fabrication process are described below.

We started from commercially available silicon-on-insulator wafers (SOITEC) with a diameter of 100 mm. Each wafer consisted of a sandwich of a 525-μm-thick "handle" wafer, a "buried" silicon oxide layer of 400 nm, and a silicon "device" layer of 340 nm thick. Both the handle wafer and the thin device layer were (100) silicon single crystals and were p-doped with a conductivity of 20−30 Ω cm. We covered both sides of the wafer with a 100-nm-thick silicon oxide layer and subsequently a 100-nm Si_3N_4 layer using chemical vapor deposition. Figure 1a shows a cross section of the wafer after this step. We then performed electron-beam lithography and subsequent CHF_3 plasma etching to open squares of ~800 μm in the silicon nitride layer covering the handle wafer. We stripped the residual resist and removed the silicon oxide in these squares with buffered hydrofluoric acid (BHF, ammonium fluoride etchant AF 87.5-12.5, Merck). Anisotropic wet KOH etching (300 g/L, 80 °C) resulted in pyramid-shaped holes through the handle wafer, as shown in Figure 1b. This is a standard microfabrication technique, based on strong differences in etch rates for the various silicon crystal directions.[26] The etching slows down significantly at the buried oxide layer, and the wafer is removed from the KOH before this layer is consumed. A quick dip in hydrochloric acid before rinsing and drying prevented residues on the wafer. We then removed the silicon nitride layer covering the device layer with a SF_6 plasma etch. Using BHF, we etched the silicon oxide layers that covered the silicon membranes on both sides. The bare silicon membrane was then thermally oxidized to form a 40-nm-thick silicon oxide layer, resulting in the structure shown in Figure 1c. In a second electron beam lithography step, we patterned a single square of ~400 nm on each membrane. This pattern was transferred to the silicon oxide layer by CHF_3 plasma etching. We then etched through the silicon device layer in 2 min using again KOH (330 g/L, 60 °C); the result is sketched in Figure 1d. Directly following this step, we rinsed in diluted hydrochloric acid and opened the pore by removing the silicon oxide using BHF. By thermal oxidation, a layer of silicon oxide was again grown on all silicon surfaces. The surface of the pore and the membrane was then covered with a silicon oxide layer 15−40 nm thick, as shown in Figure 1e and f. The final size of the pores ranges from completely closed to ~200 nm, depending on the exact size of the lithographically defined square. Up to 192 devices could be prepared on a single 4-in. wafer, with a yield greater than 90% for devices in the 50−100-nm range of sizes.

These pores could easily be located and imaged using a scanning electron microscope (SEM). Both a Philips XL30s-FEG and a Hitachi S900 microscope were used. These microscopes are known to deposit amorphous, carbon-rich contamination on the specimen, which was removed by cleaning with an oxygen plasma (Plasma Prep II, SPI Supplies).

To fabricate electrodes from the pore structures, we evaporated a 5-nm-thick chromium adhesion layer (99,998%, Kurt J. Lekser) followed by a 300-nm gold layer (99,999%, same supplier) on one side of the device. Both metals were deposited without breaking vacuum to prevent oxidation of the chromium. We found titanium to be equally effective as an adhesion layer, but all data presented herein are from devices with chromium. The gold layer was sufficiently thick to ensure complete closure of the pores, yielding well-defined, submicrometer electrodes. In the experiments, the only contact between the metal and the solution was at the nanometer-sized gold electrode at the bottom of the pyramid-shaped pore. The silicon oxide prevented contact between the solution and the silicon membrane.

Chemicals. Voltammetry measurements were carried out in aqueous solution with 1 mM ferrocenylmethyltrimethylammonium ion ($FcTMA^+$) as redox-active species and 1 M NH_4NO_3 as supporting electrolyte. $FcTMA^+$ was chosen for its uncomplicated, reversible electrochemistry and its good chemical stability in water. Details of the preparation of the FcTMA hexafluorophosphate salt can be found in the Supporting Information.

Voltammetry. Sampled-current voltammetry was performed in a two-electrode configuration using the nanoelectrode as working electrode and a commercial Ag/AgCl electrode (3 M NaCl; model RE-6, BAS) as reference. The electrode potential was varied in steps of $\Delta E = 1-10$ mV, as indicated for each individual curve. The time delay between the application of the potential step and the start of the current measurement was 0.2 s in all cases. The current was sampled over a period of 0.2 s for each point.

(26) Gribov, N. N.; Theeuwen, S. J. C. H.; Caro, J.; Radelaar, S. *Microelectron. Eng.* **1997**, *35*, 317−320.

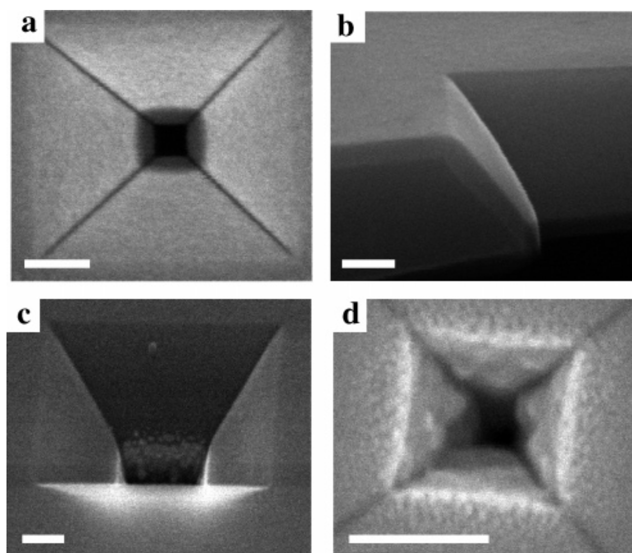

Figure 2. (a) Scanning electron micrograph of a pore prior to metal deposition (top view). The black square in the center is the actual pore. The dark gray area bordering the pore is the region where the electron beam impinges only upon the SiO_2 coating the Si membrane. The light gray square farthest from the pore is the region where the beam impinges upon the full Si/SiO_2 membrane. The dark diagonal lines occur because the pit has an inverted pyramidal shape. This is due to the KOH anisotropic etch by which the pore was formed, and the four faces correspond to the (1 $\pm$1 $\pm$1) crystal planes of the silicon. (b) Micrograph of a pore that has been cleaved to allow viewing the membrane cross section. The cleaved portion to the left of the image is closest to the viewer. The SiO_2 coating the Si membrane appears as a lighter shade. (c) Micrograph of a completed electrode viewed at a 45° angle. (d) High-resolution image of a metal electrode (top view). The scale bar in each image represents 100 nm.

Information on the measurement setup can be found in the Supporting Information.

RESULTS AND DISCUSSION

Scanning Electron Microscopy. Figure 2a shows a SEM micrograph of a pore before metal deposition. The actual dimension of each individual device was determined from such images prior to depositing the metal, thus avoiding potential carbon contamination of the electrode from the imaging process. The observed size of each pore was typically within $\pm$30 nm of the size defined by lithography. We attribute this uncertainty to residual drift during the electron beam writing process.

Figure 2b shows a SEM micrograph of a pore that was cleaved, clearly showing the cross section of the Si membrane. Such images provide detailed knowledge about the geometry of the device. In particular, note that the SiO_2 has a nonuniform thickness around sharp angles in the silicon. As a result, the sloped walls of the pore become essentially vertical at the point of greatest constriction.

Panels c and d of Figure 2 show SEM micrographs of two devices after metal deposition. The metal surface visible through the pore has the same inverted pyramid shape as the pore itself. The gold layer exhibits a rough, granular structure with bumps of ~10 nm in size; such roughness is typical for gold deposited at room temperature. In addition, small islands of metal form near the edge of the metal electrode. These appear to be electrically disconnected from the electrode proper, an observation that is supported by the voltammetry measurements discussed below.

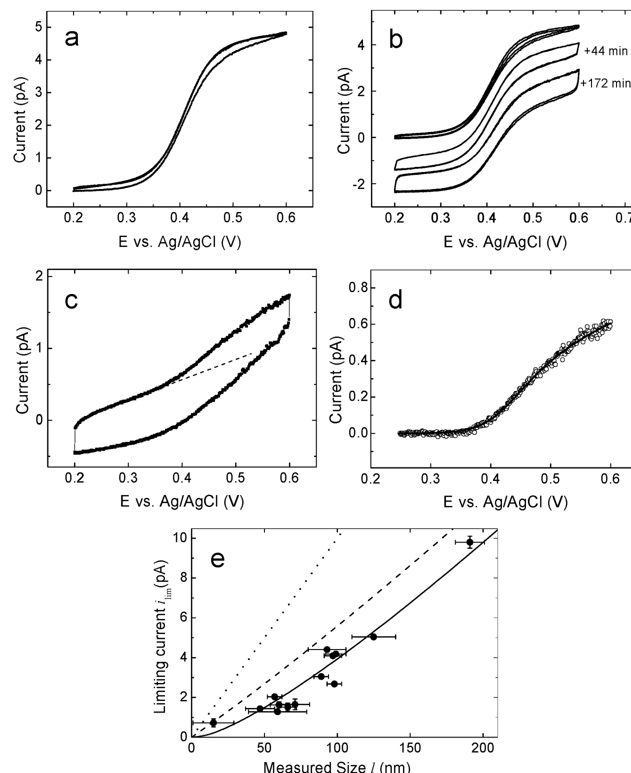

Figure 3. (a) Sampled-current voltammogram for an electrode with lateral size l = 99 nm. Forward and backward scan directions are shown. The potential step size was ΔE = 1 mV; other scan parameters are given in the Experimental Section. A fit of the forward sweep to eq 1 is also shown (solid black line, nearly indistinguishable from the data). (b) Time evolution of the signal from the device in (a). The middle and bottom cuves were measured 44 and 172 min after the top curve, respectively. Successive curves are offset by −1 pA for clarity. Each voltammogram shows two complete cycles. The step size was ΔE = 1 mV for the top curve and ΔE = 5 mV for the other curves. The contact area between the solution and the device was larger in the last curve, leading to a larger capacitive current. (c) Sampled-current voltammogram with step size ΔE = 1 mV for the smallest electrode presented here (l = 15 nm). Positive and negative scan directions are shown. A linear component of the current is due to the membrane. (d) Forward sweep from (c) with a linear background subtracted (dashed line in c). The solid line is a fit to eq 1. (e) Limiting current i_{lim} versus measured electrode size l for 14 electrodes. The lines represent calculations of the limiting current for different geometry models; see text and Figure 4 for details (dotted line, $h = h'$ = 0 nm; dashed line, h = 310 nm, h' = 0 nm; solid line, h = 310 nm, h' = 40 nm).

Sampled-Current Voltammetry. Figure 3a shows sampled-current voltammetry results on an individual electrode with lateral dimensions of 99 nm. An oxidation wave was observed at 0.41 V versus Ag/AgCl (3 M NaCl), consistent with measurements using a 5-μm-radius Pt microdisk electrode (model MF-2005, BAS). Figure 3b shows consecutive measurements using this electrode over a period of ~3 h. The magnitude of the oxidation wave decreased by 8% during this period. The same behavior was observed using the commercial Pt microdisk electrode, and we therefore attribute this slight decay to contamination from the solution.

A voltammogram for the smallest electrode investigated (15 nm) is shown in Figure 3c. In addition to the oxidation current due to $FcTMA^+$, a background current is also observed in the form of a linear dependence of the current on E at low potentials. We attribute this background current to the motion of charges in the silicon oxide layer. This interpretation is supported by several observations: First, the magnitude of the background current was independent of the size of the pore. Second, membranes in which no pore had been opened prior to metal deposition exhibited currents of similar magnitude. Third, the amount of background current was found to be sensitive to the cleanliness of the oven in which the silicon membrane was oxidized. A linear contribution to the current was therefore subtracted from the data before further analysis was conducted, as illustrated in Figure 3c,d. The existence of this background presently limits the smallest electrochemical signals that can be detected using these electrodes.

We fitted the measured voltammograms to the functional form corresponding to diffusive mass transport coupled to Butler–Volmer heterogeneous electrode kinetics,[27]

$$i(E) = i_{\text{lim}}/[1 + \exp(-F(E - E^{0'})/RT) + \lambda^{-1}\exp(-F(1-\alpha)(E - E^{0'})/RT)] \quad (1)$$

Here E is the applied electrode potential, $E^{0'}$ is the formal reduction potential, F is the Faraday constant, α is the transfer coefficient, i_{lim} is the diffusion-limited steady-state current, and λ is the so-called dimensionless heterogeneous rate constant. Fits are shown in Figure 3a and c. Because $FcTMA^+$ exhibits fast kinetics and the smallest electrodes reported here have lateral dimensions greater than 10 nm, $\lambda^{-1} < 0.1$ and heterogeneous kinetics do not affect the shape of most of our voltammograms.[2,27] We therefore concentrate in the following on the interpretation of the limiting current i_{lim}.

The limiting current i_{lim} reflects the steady-state rate of diffusion to a finite-size electrode. Figure 3e shows the measured limiting current i_{lim} versus the side length l as measured by SEM prior to metal deposition for 14 devices. i_{lim} decreases monotonically with decreasing l. If all of the devices have the same three-dimensional shape and their dimensions differ only by a scaling factor, we expect $i_{\text{lim}} \propto l$. The data do not exhibit this behavior, however: a linear fit of i_{lim} versus l does not interpolate to the origin. Instead, i_{lim} decreases faster with decreasing l than simple proportionality. We show below that this unconventional behavior can be understood by taking into account the actual geometry of the devices.

It is instructive to compare the magnitude of the measured current with what would be expected for a conventional shrouded disk electrode of radius a. For this geometry, $i_{\text{lim}} = 4FDc_0a$, where D and c_0 are the diffusion constant and bulk concentration of $FcTMA^+$, respectively.[2] The value $FDc_0 = 50$ pA/μm was determined by measuring i_{lim} for a microdisk electrode with $a = 5\ \mu$m. The observed limiting current for a $l = 100$-nm electrode, ~4 pA, thus corresponds to the limiting current of a disk electrode with radius $a = 18$ nm. This reflects the fact that the pore electrode is less accessible to solution. The average current density i_{lim}/A, where $A = 2.46l^2$ is the surface area of the electrode in contact with solution, is correspondingly reduced: an electrode with $l = 100$ nm has the same average current density (or, equivalently, the same mean mass-transfer coefficient i_{lim}/FAc_0) as a disk electrode with $a = 390$ nm.

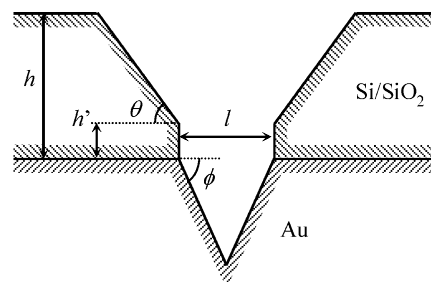

Figure 4. Geometry model used for the simulations. The figure is a two-dimensional cut through the center of the structure; the calculation is performed in three dimensions.

Theoretical Determination of the Limiting Current. At sufficiently high overpotential, the redox current at an ultramicroelectrode is limited by mass transport and can be determined from solutions to the diffusion equation, $\partial c(\mathbf{r})/\partial t = D\nabla^2 c(\mathbf{r})$. Here $c(\mathbf{r})$ is the local concentration of $FcTMA^+$. The corresponding electrical current density is $FD\nabla c(\mathbf{r})$.

A three-dimensional geometry model of our devices is shown in Figure 4. The parameters in this model are the thickness of the insulating membrane h (310 nm in our experimental devices), the lateral size of the pore l (15–200 nm), the angles θ (54.7° for the (1 1 1) planes of silicon), ϕ (66 ± 5° as determined from SEM images at different angles), and the thickness h' of a region near the electrode where the silicon oxide walls rise vertically. The latter is due to the finite thickness of the silicon oxide around the pore. From SEM images such as Figure 2b, we estimate $h' = 40$ nm. The main residual approximations in this geometry model are that the roughness of the silicon oxide and of the gold (several nm), as well as the rounding of sharp edges, have been ignored. Note that the geometry of each device depends on its lateral size l since the thickness of the membrane (parameters h and h') is independent of l. For example, halving l leads to a different geometry in which h/l and h'/l are doubled.

Using finite-element methods (Supporting Information), we obtained numerical solutions to the diffusion equation for the geometry of Figure 4. The computed values of the limiting current i_{lim} versus electrode size l are shown in Figure 3c together with the experimental data. The computed values of the limiting current are in agreement with the data within experimental error. For comparison, Figure 3c also shows calculations for simpler geometries than those of Figure 4, namely, the cases where the insulating membrane is infinitely thin ($h = h' = 0$ nm) and the case where the vertical walls at the bottom of the pore are neglected ($h = 310$ nm, $h' = 0$ nm). These simplified geometries do not agree with the experimental observations, instead predicting $i_{\text{lim}} \propto l$ and overestimating the magnitude of i_{lim}. Further details about the origin of this behavior are discussed in the Supporting Information.

CONCLUSIONS

We have demonstrated a new method for fabricating metal electrodes with lateral dimensions below 100 nm using lithography

(27) Zoski, C. G. In *Modern Techniques in Electroanalysis;* Vanysek, P., Ed.; Wiley: New York, 1996; pp 241–312.

techniques. This approach has several benefits. First, the metal layer is deposited in the last fabrication step from a pure target under high-vacuum conditions and is thus never exposed to contaminants during electrode fabrication. Second, the electrodes are insulated using silicon oxide, making them compatible with a broad range of solvents. Third—and most important for analytical applications—the lithography-based approach provides detailed information on the geometry of the devices that can be independently validated using voltammetry.

Several improvements to the devices described here can be envisaged. First, their geometry could be modified so that the metal electrode presents a convex or flat surface to the solution, facilitating diffusion. This can be achieved by filling the pore with a sacrificial material before metal deposition. Second, the thickness of the silicon oxide away from the pore could be increased to reduce the background current associated with this layer. Third, the size of the electrodes could be decreased further. Since this is determined by the size of the pore in a silicon oxide membrane, and a technique for controllably fabricating such pores with a 2-nm diameter has recently been reported,[28] we believe that electrodes with a diameter of a few nanometers can be fabricated using this process.

(28) Storm, A. J.; Chen, J. H.; Ling, X. S.; Zandbergen, H. W.; Dekker: C. *Nat. Mater.* **2003**, *2*, 537−540.

ACKNOWLEDGMENT

We thank Bernadette M. Quinn for useful discussions. This research was supported by Stichting voor Fundamenteel Onderzoek der Materie (FOM), The Netherlands Organization for Scientific Research (NWO) and by NanoNed, a program of the Ministry of Economic Affairs of The Netherlands.

SUPPORTING INFORMATION AVAILABLE

Additional details on chemical preparation, the electrochemical measurement apparatus, numerical methods, and interpretation of the calculations. This material is available free of charge via the Internet at http://pubs.acs.org.

Received for review July 9, 2004. Accepted January 6, 2005.

AC0489972